

The effect of external electric fields on Si with superconducting Ga nano-precipitates

The effect of external electric fields on silicon with superconducting gallium nano-precipitates

Brandur Thorgrimsson,^{1, a)} Thomas McJunkin,¹ E. R. MacQuarrie,¹ S. N. Coppersmith,^{1, 2} and M. A. Eriksson¹

¹⁾*University of Wisconsin-Madison, Madison, WI 53706, USA*

²⁾*University of New South Wales, Sydney, NSW 2052, Australia*

(Dated: 3 February 2022)

Motivated by potential transformative applications of nanoelectronic circuits that incorporate superconducting elements, and by the advantages of integrating these elements in a silicon materials platform, we investigate the properties of the superconductivity of silicon ion-implanted with gallium. Here we measure 40 different samples and explore both a variety of preparation methods (yielding both superconducting and non-superconducting samples), and the reproducibility of one of the preparation methods yielding superconducting samples. While we find agreement with the existing literature that superconducting effects are visible in this system, we also find that this superconductivity is not influenced by voltages applied to a top gate. The superconductivity in this materials system is not gateable for applied electric fields as large as 8 MV/cm. We also present results of scanning transmission electron microscopy imaging of some of the same samples for which we report electronic characterization. In agreement with the existing literature, we find that the presence of Ga precipitates is essential to the presence of a superconducting transition in these samples. However, we also find evidence for large inhomogeneities in this system, which we discuss in connection with the lack of gateability we report here.

^{a)}Electronic mail: thorgrimsson@wisc.edu

I. INTRODUCTION

The integration of superconducting and semiconducting nanostructures has the potential to enable interesting and novel quantum devices¹⁻³. One advantage of such integration is the ability to modulate superconductivity with a gate voltage, which has been demonstrated in both III-V and II-VI semiconductors, including InAs⁴, InSb⁵, and HgTe⁶, all of which form low Schottky barrier contacts with superconductors. Recently, the superconducting proximity effect has also been observed in compressively-strained Ge grown on relaxed SiGe⁷.

The promise of these devices combined with the technological importance of silicon semiconductor devices motivates us to investigate superconductivity in silicon. Although silicon has low intrinsic spin-orbit coupling, it remains an important candidate for applications requiring spin-orbit interactions, because artificial spin-orbit coupling can be introduced using nanomagnet arrays, which have been proposed to enable superconducting silicon nanowires to support Majorana zero modes⁸⁻¹⁰.

A challenge in working with superconductivity in silicon is that the Fermi level is pinned near neither the conduction nor valence bands¹¹ making it difficult to proximitize undoped silicon. Very high doping has been shown to circumvent this problem. The superconducting proximity effect has been observed in silicon highly doped with boron^{12,13}. And at very high boron concentrations, silicon itself becomes superconducting at temperatures below 0.35 K¹⁴.

An alternative approach to generating superconductivity in silicon is the implantation of Ga to form nanoprecipitates, and this method has the advantage of observed critical temperatures as high as ~ 7 K¹⁵⁻²¹. This method depends on annealing of the sample after Ga implantation, which causes the Ga to diffuse, resulting in both clusters and a wide range in nominal carrier density^{16,17}.

Encouraged by the gateability of the proximity effect in III – V materials^{2,4,5}, II – VI materials⁶ and germanium^{7,22}, and by the high T_C of superconductivity in Si:Ga, we here investigate superconductivity in silicon highly doped with Ga under a wide range of annealing conditions and under large applied electric fields. By studying two sets of samples, the first with a range of processing conditions and the second with a single set of processing conditions, we address the important open question of the controllability and repeatability of the generation of superconductivity in silicon through the annealing of silicon highly doped with gallium. In studying the first set, we find agreement with literature results that there is a mid-range annealing temperature, in our experiments between 450 and 550 °C, that produces superconductivity in Si:Ga¹⁵. We further test the

gateability of the conductivity using a gate electrode separated from the Si:Ga by SiO_2 , with thicknesses ranging from 30 nm to 200 nm, allowing us to apply electric fields as large as 8 MV/cm. At temperatures corresponding to the superconducting transition edge, such fields produce very small changes in resistance, consistent with zero to within the uncertainty of the measurement.

We also find that there is a large variability in this process, such that samples on the same chip and processed identically yield different results. Such results suggest inhomogeneity, and we report Hall measurements of Si:Ga samples that reveal anisotropy consistent with such inhomogeneity.

Based on Hall measurements of the hole carrier density in two samples with partial superconducting transitions, the carrier densities are low enough that the electric fields applied would be expected to change the carrier density by $\sim 10\%$, greater than the observed proportional change in conductivity. Additionally, we measure non-zero Hall voltages at zero external magnetic field. Both observations are consistent with a nonuniform distribution of charge carriers.

We investigate the reproducibility of a single preparation method by measuring the resistance of these samples at liquid helium temperature, T_{LHe} , and we find wide variations between the resistances of 21 nominally identical samples. For some of these devices we find that the resistance at T_{LHe} is more than 6 orders of magnitude lower than the room temperature resistance while for others we find that their resistance at T_{LHe} is only an order of magnitude lower than the room temperature resistance.

We confirm the presense of gallium nano-precipitates in these samples through TEM imaging. By comparing the temperature dependence of the resistance in samples which have had none, some, or all of their gallium nano-precipitates removed by chemical etching, we find that the supercurrent flows predominantly near the Si/ SiO_2 oxide interface. Finally, we report that voltage-gateable superconductivity is not found in any sample. The large sample-to-sample variations of the conductivity are consistent with superconductivity that occurs in gallium precipitates as opposed to proximity-induced superconductivity in the silicon.

The paper is organized as follows: section 2 describes in detail the various sample preparation processes and the measurement procedures. Section 3 describes the main results including data relevant to gateability under applied electric fields and the homogeneity of the materials. Section 4 discusses the implications of the measurement results from this large set of samples. The appendices present additional details of the sample preparations and the experiments.

II. METHODS

A. Sample preparation

The sample preparation procedure is illustrated in figure 1. At 300 K a nominally 30 nm layer of SiO_2 is sputtered onto 3" float-zone n-type (100) silicon wafers (from WaferPro) with resistivity $> 10 \text{ k}\Omega\text{cm}$ (see figure 1(b)). Gallium ions with energy 80 keV and dose $4 \times 10^{16} \text{ cm}^{-2}$ then are implanted at a 7° angle to the sample normal (figure 1(c)); to avoid overheating the substrate, during the ion implantation the ion beam current is kept below $0.5 \mu\text{Acm}^{-2}$. The wafers are diced into $5 \times 5 \text{ mm}^2$ dies, and individual dies undergo a rapid thermal anneal (RTA) at a variety of temperatures and annealing times (figure 1(d)). Table I provides a list of the 40 samples measured in this work, including descriptions of the annealing protocols used, the number of samples measured for each protocol, the types of measurements performed on each sample group, the chemical etchant used to etch devices for each method, the ohmic contact metal, and the annealing gas used. The annealing conditions chosen span a range that yields both superconducting and non-superconducting samples. In general, superconductivity is found in samples annealed at 450-550 °C for 30-900 s, with annealing temperatures measured using a thermocouple that touches the backside of the samples during the anneal.

Two oxide steps were used in the fabrication of the devices reported in this paper. First, all devices had 30 nm of SiO_2 sputtered onto them before the Ga ion implantation. This oxide layer protects the silicon during the ion implantation and is partially ablated during the implantation. Second, different amounts of additional SiO_2 were added during subsequent processing for different devices to serve as a gate oxide. Because we use the final oxide thickness to determine the external electric fields applied to the devices, we discuss how the final oxide thickness is determined in Appendix B.

For the devices listed in Table II with a 100 nm or 200 nm additional oxide thickness, devices were etched, following the ion implantation, using a fluorine based plasma etch. After sputtering the additional SiO_2 gate oxide, a buffered oxide etch (BOE), hydrofluoric acid 20:1, was used to etch through the oxide over ohmic contact regions. Tungsten was then sputtered (170 nm) over the entire wafer, lithography was performed, and the tungsten was etched using a fluorine-based plasma etch to create metallized ohmic contacts and top gates. The wafers were diced into $5 \times 5 \text{ mm}^2$ dies, and finally individual dies underwent different RTA processes. In Ref. 17 a variety of RTA

The effect of external electric fields on Si with superconducting Ga nano-precipitates

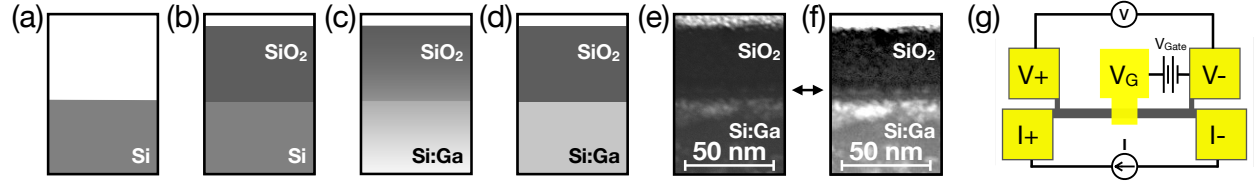


FIG. 1. (a)-(d) Schematic images of the substrate at different stages during fabrication. (a) A (100)-oriented Si wafer with resistivity $> 10 \text{ k}\Omega\text{cm}$ is (b) sputtered with a 30 nm thick layer of SiO₂. (c) Gallium is then ion implanted with energy of 80 keV and a dose of $4 \times 10^{16} \text{ cm}^{-2}$ at a 7° angle from the sample normal. The ion beam current was kept below $0.5 \mu\text{Acm}^{-2}$. (d) Finally, the substrate undergoes a rapid thermal anneal (RTA). (e) Scanning transmission electron microscope (STEM) image of a sample annealed at 550 °C for 30 s. The oxide thickness of this sample is $\sim 40 \text{ nm}$. During the device fabrication (after ion implantation) this sample had 30 nm of SiO₂ sputtered onto it in addition to the 30 nm thick SiO₂ sputtered onto it prior to ion implantation. During the ion implantation a portion of the oxide is milled away resulting in a final oxide thickness of $\sim 40 \text{ nm}$. (f) The same image as in (e), but at an adjusted contrast. The arrow highlights the boundary in the oxide layer between the oxides sputtered before and after ion implantation. (g) Schematic image of devices used to measure the electrical transport properties. Four-probe resistance measurements were performed by sourcing current from I+ to I- and measuring the voltage between V+ and V-. An oxide separates the current channel from a top gate. Measurements that attempt to modify the conductance of the current channel using external electric fields are performed by applying a voltage, V_{Gate} , to the top gate, referenced to V-.

procedures were used to modify the carrier concentration; low concentrations yielded insulating samples, and high concentrations yielded superconducting samples. Here we make use of similar annealing procedures, which are described for each sample in Table 1. Most of the RTA steps were performed in a flowing nitrogen atmosphere (1 sccm of N₂) and ranged in temperature from 550 °C to 650 °C and in duration from 15 s to 60 s. We also made use of a flowing forming gas (FG, 1 sccm) anneal at 450 °C for 900 s anneal.

For the devices listed in Table II with 30 nm and 40 nm gate oxide thickness and in figures 3, 4 & 6, after the ion implantation, the samples were diced into $5 \times 5 \text{ mm}^2$ dies and then were annealed using an RTA process, for 30 s at 550 °C in a flowing nitrogen atmosphere (1 sccm of N₂). After the annealing, multiple devices were etched for four-probe electrical measurements using a chlorine-based plasma etch. These devices had a 500 μm long and 20 μm wide channel between source

TABLE I. **Summary of sample preparations and measurements.** The 40 samples reported in this paper were prepared using 5 different annealing methods, with temperatures ranging from 450 °C to 650 °C, and duration ranging from 15 s to 900 s. Anneals done at 450 °C were performed in a forming gas atmosphere while anneals done at 550 °C and above were performed in a nitrogen gas atmosphere. The table also shows the number of samples measured for each annealing method, the measurements performed on each sample group, the chemical etchant used to etch devices for each method, the ohmic contact metal, and the annealing gas used.

Method	Annealing		Number of Samples	Measurements	Device Plasma Etchant	Ohmic Metal	Annealing Gas
Label	Temp (°C)	Time (s)					
650/30	650	30	5	Gating	Fluorine	Tungsten	N2
650/15	650	15	1	Gating	Fluorine	Tungsten	N2
550/60	550	60	4	Gating	Fluorine	Tungsten	N2
450/900	450	900	4	Gating	Fluorine	Tungsten	FG
550/30	550	30	3	Location of superconductivity and gating	Chlorine	Ti/Au	N2
550/30	550	30	21	Reproducibility	Chlorine	Ti/Au	N2
550/60	550	60	2	Hall measurements	Fluorine	Tungsten	N2

and drain (schematic shown figure 1(g)). BOE was used to etch through the oxide over the ohmic contact regions before the ohmics were metalized by evaporating Ti(20 nm)/Au(140 nm) using an e-beam evaporator.

To determine the location of superconductivity within the sample heterostructures, a few dies, reported in figure 4, were processed further. BOE was used to remove the oxide in a $10 \times 20 \mu\text{m}^2$ area of the current channel, after which an additional 30 nm of SiO_2 was sputtered and then a Ti(20 nm)/Au(280 nm) top gate was evaporated on top of the exposed region. Finally, a BOE was used to re-expose the metalized ohmic contacts. For comparison with the devices that underwent oxide removal, Ti/Au top gates were also evaporated on some devices that had not had their oxide removed (these devices are categorized with the "Location of superconductivity" devices in

Table I); figure 1(g) shows a schematic image of these devices.

B. STEM sample preparation and imaging

Scanning Transmission Electron Microscopy (STEM) samples were prepared using a Helios G4 UX DualBeam System. During the sample preparation an electron-beam was used to deposit a thin ($\sim 200\text{nm}$) platinum cover layer, a thicker (few μm) cover layer was then deposited using an ion-beam. This procedure was used because the cover layer protects the surface of the STEM sample from the ion-beam used to mill out the STEM sample. STEM images (not shown) of samples that had their initial cover layer deposited using an ion-beam showed significant damage $\sim 30\text{ nm}$ from the surface and into the gallium doped silicon beneath the Si/SiO₂ interface. Imaging was performed using a FEI Titan 200 keV STEM using a high angle annular dark field (HAADF) image detector.

C. Electrical measurements

Measurements were performed in an Oxford Teslatron cryostat, in liquid helium dewars, in a Quantum Design Physical Properties Measurement System (PPMS), and in a Janis dilution refrigerator (DR). For measurements in the Oxford Teslatron, helium dewars and Janis DR, a Keithley 2400 source meter was used to source current and measure voltage. In the PPMS a Keithly 6221 current source was used to source current and the voltage was measured using a Keithley 2182 nanovoltmeter. For all experimental setups a Keithley 2400 source meter was used to apply top gate voltages and to measure the top gate leakage current.

As discussed above, the range of sample preparation conditions was chosen to yield both non-superconducting and superconducting samples. In general, non-super-conducting samples have low carrier concentrations and superconducting samples have high carrier concentrations. For the devices that superconduct we attempted to turn the device non-superconducting by reducing the density of carriers with an external electrical field. For p-type dopants, such as gallium, this means applying a positive gate voltage to reduce the number of holes. For non-superconducting devices we attempted to induce superconductivity by increasing the number of holes by applying a negative voltage. For both superconducting and non-superconducting devices, the top gate voltages were increased until breakdown voltages were reached, which we determined by monitoring the

leakage current through the top gate while simultaneously monitoring the four probe resistance of the device. To compare devices with different oxide thicknesses we convert the applied top gate voltage into applied external electric field by dividing the applied top gate voltage with the oxide thickness. We compare the conductance change at an external electric field of 1 MV/cm across multiple devices.

Hall measurements were performed in a Janis DR on samples with a square van der Pauw geometry²³. The Hall voltage (V_H), at an applied current (I), was measured as a function of external perpendicular magnetic field (B_\perp). The formula, $n_{2D} = -IB_\perp/(eV_H)$, where e is the elementary charge, was then used to extract the carrier type and sheet density per unit area (n_{2D}).

III. RESULTS

A. Superconducting transition

Table II describes the annealing protocol, oxide thickness, top gate area, the experimental conditions, the maximum applied electric field and the raw resistance data for each sample shown in figure 2. The annealing protocols range from 450°C to 650°C in temperature and from 15 s to 900 s in duration, the oxide thickness ranges from 30 nm to 200 nm and the gate area ranges from 4 μm^2 to 225 μm^2 . The color of the data points in figure 2 identifies the different conductance behaviors of different devices when cooled below 7 K. Devices either show a full superconducting transition (dark gray), show a partial superconducting transition to a finite resistance value (light gray), or show no superconducting transition (black). In general, we find that higher temperatures result in non-superconducting samples.

Figure 2(a) shows resistance vs. temperature measurements for 3 different devices in the temperature range of 5.5 to 7.5 K. These three devices are identified with a \blacklozenge , \star or \blacksquare in Table II and were annealed using 550°C for 60 s(\blacklozenge , \blacksquare) and 450°C for 900 s(\star).

These devices demonstrate two different behaviors observed in these experiments: the device identified by \blacklozenge shows a full superconducting transition, while the devices identified by \star and \blacksquare show partial superconducting transitions to (different) finite conductances. Devices with no signs of superconductivity were also measured. We note that the devices identified by \blacklozenge and \blacksquare underwent the same annealing procedure but show different conductance behaviors.

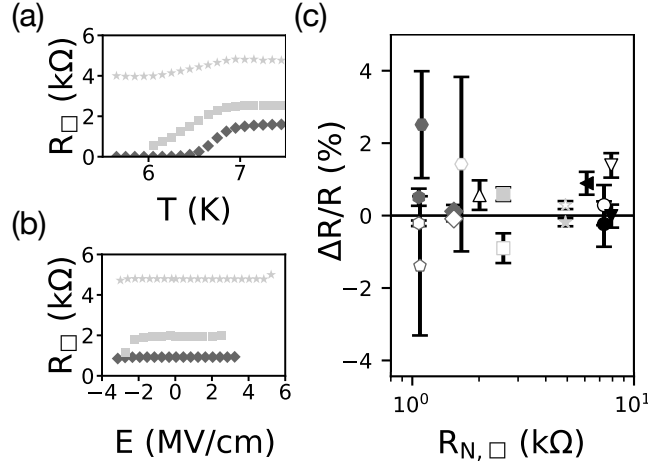


FIG. 2. External electric fields change the conductivity by less than 3%. a) Resistance per square (R_{\square}) vs. temperature (T) for the three devices identified by ◆, ★, ■ in Table II. The devices show either a full (◆) or partial (★, ■) superconducting transition when cooled below 7 K. b) Resistance per square (R_{\square}) vs. external electric field (E) of the same devices as in (a), identified by ◆, ★, ■ in Table II. These measurements were performed at the superconducting transition: 6.6 K (■) and 6.75 K (◆, ★). Less than a 3% change is observed in the resistance of the device until after dielectric breakdown, where additional current enters the device channel through the top gate and the model of four probe resistance measurement used to determine the resistance no longer applies to the system. c) Measured proportional change in device resistance ($\Delta R/R$) when an externally applied electric is changed from 0 to 1 MV/cm vs. the normal resistance per square ($R_{N,\square}$) of the device. A unique symbol represents each device. That symbol, annealing method, oxide thickness, top gate area, the experimental conditions, the maximum applied electric field, resistance data and the temperature at which gating electric fields are applied to each sample are summarized in Table II. We use black symbols to identify non-superconducting samples, light gray symbols to identify samples with a partial superconducting transition, and dark gray symbols to identify samples with a complete superconducting transition. The precise geometries if the lithographically-defined Hall bars are all qualitatively the same as the device described in figure 1(g) and the main text. The value of the voltage at which the external electric field is 1 MV/cm is calculated by multiplying the electric field by the oxide thickness between the current channel and the top gate. For superconducting devices where we want to decrease the number of holes a positive voltage is used. For normal devices where we want to increase the number of holes a negative voltage is used. The plotted percentage change in resistance is calculated by dividing the difference in resistance at an external field of 1 MV/cm and no external field by the average resistance measured between those two voltage values. The maximum change in resistance observed across the devices measured was less than 3%.

B. External electric fields change the conductivity by less than 3%

Figure 2(b) shows measurements of a device resistance as a function of applied external electric field for the devices identified by ◆, ★ and ■ in Table II. These measurements were performed at the superconducting transition: 6.6 K (■) and 6.75 K (◆, ★). The applied external electric field, for these three devices, are swept from; -3 to 3 MV/cm (◆), -2 to 2 MV/cm (■), and -3 to 4 MV/cm (★) before gate oxide breakdown is reached. The changes in resistances are clearly

negligible until the breakdown voltages. After that voltage, current flows into the substrate from the top gate, making the four probe resistance measurement used to determine the resistances of the devices inaccurate. The observed resistance changes in each device before breakdown are 0.85 ± 0.23 % (■), -0.34 ± 0.13 % (★), and 0.03 ± 0.12 % (◆).

To summarize multiple datasets like the ones shown in figure 2(b) we show in figure 2(c) the proportional resistance change at 1 MV/cm vs. normal resistance per square, for multiple devices. The maximum change in resistance observed across the measured devices is less than 3%. The normal resistance per square for the devices shown ranges from 1 to 10 k Ω . Devices that have a full superconducting transition have lower normal resistance than devices that had a partial or no superconducting transition and devices that have a partial superconducting transition have a lower normal resistance than non-superconducting devices (with one exception, see Δ in figure 2(c)). The different annealing methods used during fabrication, oxide thicknesses, and top gate areas for the different devices are described in Table II. For each device, electric fields are applied until a breakdown field is reached. The maximum electric field we reach in our experiments is 8 MV/cm, and even at these higher electric fields we find no significant change in resistance across the measured devices. We note that top gates with smaller lateral dimensions are generally expected to yield higher breakdown fields, as a smaller area decreases the chance of having a defect in the oxide that may lower the breakdown field. We also note that the data for the proportional change in resistance ($\Delta R/R_0$) in Table II is the value at 90% of the breakdown field (E_{BD}) and not at 1 MV/cm which is shown in figure 2. Table II also tabulates the temperature at which we attempted to gate each device; superconducting devices were measured at or below the superconducting transition, while samples labelled non-superconducting showed no superconducting transition down to at least 4 K.

C. Resistance of nominally identical samples varies by many orders of magnitude below T_C

Through our gating attempts we found that nominally identical devices had a greater than expected (>few 10%) variation in resistance below T_C . To determine the extent of this variation we prepare 21 nominally identical devices annealed at 550°C for 30 s and measure them in liquid helium at 4.2 K. A resistance drop is observed in all devices when they are cooled below the superconducting transition temperature, $T_C \approx 6.7$ K (like the example shown in figure 2(a)). Figure 3 shows a histogram of the four probe resistance R_{4K} at a temperature $T = 4.2$ K of these 21 nominally identical devices. As shown in figure 3, the resistance at $T = 4.2$ K varies by orders of

TABLE II. Summary of samples fabricated and results of attempts to perform electrical gating for samples shown in figure 2. This table relates each unique symbol in figure 2 to the corresponding sample and shows the raw data for the samples we attempted to gate. The table columns are: Symbol (Symb.) used to identify the sample in figure 2, The annealing method (Meth.), temperature/time in degrees Celsius and seconds, described in Table I, the presence of a superconducting transition (S.C. Tr.) when cooled below 7 K, indicating if there was no transition (NO, Black symbols), a partial transition to a finite value (YES(P), light gray symbols) or a complete transition (YES, dark gray symbols). the minimum temperature reached during the experiment (T_{\min}), the resistance at T_{\min} ($R(T_{\min})$), the normal state resistance (R_N), the temperature at which we attempted to gate the sample (T_{Gate}), the gate oxide thickness (d_{ox}), the external electric field breakdown value (E_{BD}), the area of the top gate the external electric field was applied to (A_{Gate}), the average and standard deviation in resistance when applying external electric fields, (R_0) and (σ_{R_0}), the change and proportional change in resistance from no external electric field to 90% of the breakdown field value (ΔR) and ($\Delta R/R_0$). We note that the value of $\Delta R/R_0$ shown in figure 2, is the value of $\Delta R/R_0$ at 1 MV/cm. For samples that have a S.C. Tr.; R_N is measured at 7.5 K, for samples without a S.C. Tr.; R_N is measured at T_{\min} . For all samples the resistance change was less than 3%, even when external electric fields of up to 8 MV/cm were applied.

Symb.	Meth.	S.C. Tr.	T_{\min} (K)	$R(T_{\min})$ ($k\Omega/\square$)	R_N ($k\Omega/\square$)	T_{Gate} (K)	d_{ox} (nm)	E_{BD} (MV/cm)	A_{Gate} (μm^2)	R_0 ($k\Omega/\square$)	σ_{R_0} (Ω/\square)	ΔR (Ω/\square)	$\Delta R/R_0$ (%)
●	650/30	NO	4	7.33	7.33	4	100	3.39	180	7.77	50	38	0.48%
○	650/30	NO	4	7.33	7.33	4	100	1.9	225	7.76	42	37	0.48%
▼	650/30	NO	4	7.90	7.90	4	100	2.27	48	8.16	32	129	1.58%
▽	650/30	NO	4	7.90	7.90	4	100	1.78	60	8.15	98	161	1.98%
△	650/30	NO	4	2.01	2.01	3.9	100	1.98	225	2.05	8	20	0.98%
◀	650/15	NO	3.9	6.06	6.06	4	200	2.85	180	6.29	123	47	0.75%
■	450/900	YES(P)	6	0.49	2.52	6.6	200	2.3	4	1.96	4.35	17	0.85%
□	450/900	YES(P)	6	0.49	2.52	6.6	200	6	16	1.96	5.6	-1.39	-0.07%
◆	450/900	YES	5.6	0.00	1.50	6.75	200	2.52	4	0.92	1.23	0.32	0.03%
◇	450/900	YES	5.6	0.00	1.50	6.75	200	5.19	16	1.00	0.6	-0.25	-0.03%
★	550/60	YES(P)	5.6	4.00	4.82	6.75	200	5.21	8	4.79	5.9	-16	-0.34%
☆	550/60	YES(P)	5.6	4.00	4.82	6.75	200	3.62	16	4.80	6.26	12	0.24%
⬢	550/60	YES	5.6	0.03	1.05	6.75	200	2.81	36	0.53	1.2	2.69	0.51%
⬡	550/60	YES	5.6	0.03	1.05	6.75	200	2.59	64	0.52	0.43	0.19	0.04%
⬠	550/30	YES	2.5	5.0E-06	1.04	4	40	3.6	100	2.5E-4	6.5E-2	2.3E-3	0.87%
⬢	550/30	YES	2.5	2.0E-06	1.06	5	40	5	100	2.6E-4	4.5E-3	4.5E-3	1.69%
⬡	550/30	YES(P)	4.5	0.15	1.60	5	30	8	100	0.95	16	19.75	2.09%

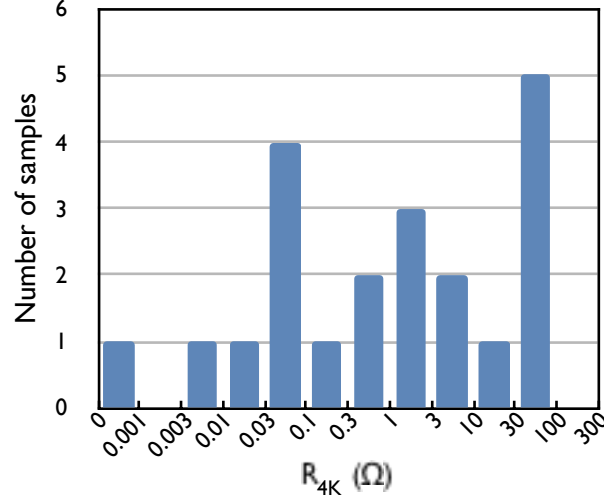


FIG. 3. **The electrical transport properties of nominally identical devices can vary by many orders of magnitude.** A histogram of the resistance at $T = 4.2$ K, R_{4K} , of 21 nominally identical devices, annealed at 550°C for 30 s. The labels are the resistance boundaries between each column. The room temperature resistances of these devices are $984 \pm 108 \Omega$. Every device showed a superconducting transition when cooled below 7 K (see, e.g., figure 2(a)), with conductances below the transition at least an order of magnitude greater than the normal state conductance.

magnitude, from <1 m Ω to $\sim 90 \Omega$. We note that such variations are not unexpected in the presence of inhomogeneity in samples consisting of a percolative superconducting network, as has been suggested (Ref. 24) could be present in this materials system. We also note that a quarter of the devices have a resistance below 0.06Ω , another quarter a resistance between 0.06 and 1Ω , a third quarter a resistance between 1 and 30Ω , and a quarter of the devices have a resistance greater than 30Ω . This variation is observed across nominally identical devices, some located on the same 5×5 mm² die. The room temperature resistances of these 21 nominally identical devices are $984 \pm 108 \Omega$ and a similar ($\sim \pm 10\%$) variation was observed in the resistances of these devices just before they were cooled below the superconducting transition. We note that even for the highest resistances at $T = 4.2$ K, the resistance drop observed when the devices are cooled below T_C is greater than an order of magnitude.

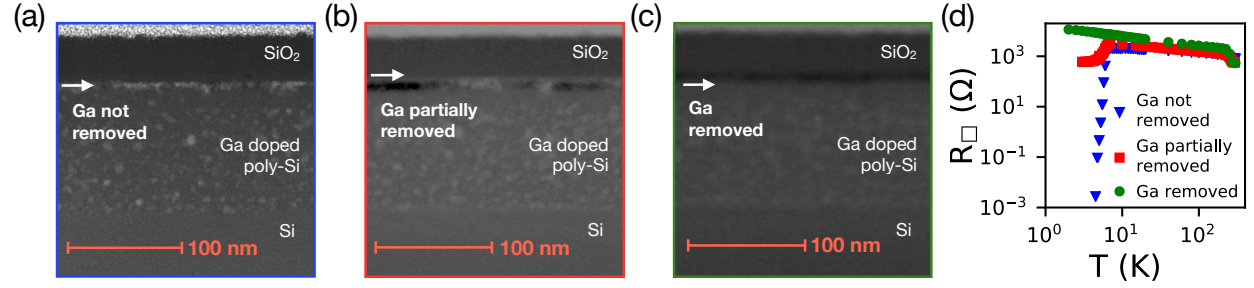


FIG. 4. The electrical transport properties are dominated by gallium precipitates located at the Si/SiO₂ interface. (a) STEM image of a device not modified with respect to what is described in figure 1, i.e., no BOE etching performed. Energy dispersive x-ray spectroscopy (EDX) measurements (not shown) confirm that both the bright spots at the Si/SiO₂ interface and the speckles below the interface are gallium. (b) STEM image of a device on a die where a BOE etch resulted in a partial removal of the gallium precipitates at the Si/SiO₂ interface. (c) STEM image of a device on the same die as the image shown in (b), but where the same BOE etch resulted in a complete removal of the gallium precipitates at the Si/SiO₂ interface. (d) Resistance vs. temperature for all 3 devices. These three devices, with different amounts of gallium precipitates present at the Si/SiO₂ interface, show different behaviors when cooled below 7 K. For an unetched device (blue triangles), a full superconducting transition is observed; for a device where the gallium precipitates at the Si/SiO₂ interface were partially removed using BOE (red squares, same device as a STEM image is shown of in (b)), a resistance drop to a finite value is observed; and for a device where the gallium precipitates at the Si/SiO₂ interface were completely removed using the same BOE etch (green circles, same device as a STEM image is shown of in (c)), a continued rise in resistance is observed.

D. Structural and transport studies of samples with different surface treatments.

Previous work has demonstrated that during the RTA process the implanted gallium forms precipitates²⁵ and migrates towards the Si/SiO₂ interface¹⁵. To connect the results reported above to these same structural features, we study 3 devices, fabricated on two dies, which have different densities of Ga precipitates at the Si/SiO₂ interface. The first STEM image, shown in figure 4(a), is of a die that did not undergo a BOE etch and shows an increased concentration of gallium precipitates at the Si/SiO₂ interface compared to the surrounding material. Figure 4(b) & (c) show STEM images of the other two devices. Both are from the same die and underwent the same BOE etch. For the second device, shown in figure 4(b), this etch resulted in partial removal of the gallium precipitates at the Si/SiO₂ interface; for the third device, shown in figure 4(c), this etch resulted in

a complete removal of the gallium precipitates at the Si/SiO₂ interface. Electrical measurements were performed on these devices before STEM samples were prepared and imaged. Gallium precipitates are apparent in these STEM images, which also show mono-crystalline undoped silicon (at the bottom), polycrystalline silicon with gallium nano-precipitates (in the middle), and increased or removed gallium nano-precipitates at a Si/SiO₂ interface, and SiO₂ (near the top). At the very top of the images a glimpse of either a platinum cover layer, figure 4(a), or a titanium sticking layer for the top gate, figures 4(b) and (c), can be seen.

Figure 4(d) shows resistance vs. temperature measurements for these three different devices in the temperature range 2 to 300 K. The samples were each annealed at 550°C for 30 s, and as can be seen in figure 4(d), such samples show different behaviors as they are cooled below 7 K. A device where gallium precipitates at the Si/SiO₂ interface were partially removed (red squares) shows a resistance drop to a fixed value; for the device where all the gallium precipitates at the Si/SiO₂ interface were removed (green circles) the resistance continues to rise; and the unetched device (blue triangles) shows a full superconducting transition. These measurements show that the superconductivity observed in these samples is observed only in the presence of the gallium precipitates at the Si/SiO₂ interface, as completely removing them results in a continued resistance rise upon decreasing temperature, consistent with previous observations in this material system¹⁵.

E. Hall measurement data

Figure 5(a) shows resistance vs. temperature measurements and Hall measurements for two devices. Both samples show a partial superconducting transition to a finite resistance value when cooled below 6.5 K. Figures 5(b) & (c) show the Hall measurement data for two devices on which Hall measurements were performed at 8 K. Both samples were annealed at 550°C for 60 s. For the first (second) sample a $-102 \mu\text{V}$ ($-90 \mu\text{V}$) change in Hall voltage is observed when the perpendicular magnetic field is changed from -1 to 1 T when sourcing a $10 \mu\text{A}$ longitudinal current. A longitudinal resistance per square of $1.80 \text{ k}\Omega$ ($1.86 \text{ k}\Omega$) was measured at 8 K. The negative Hall slope shows that holes are the majority carrier. If the sample is a uniform sheet then the carrier density of device 1(2) can be calculated to be 1.2×10^{14} (1.4×10^{14}) cm^{-2} . However, we note that the Hall voltage at zero external magnetic field is offset from 0 V by 0.35 mV (see figure 5(b)) and -3.8 mV (see figure 5(c)), respectively, and that if a sample being measured with a Hall measurement is a uniform sheet then the Hall voltage should be 0 V at zero external magnetic field.

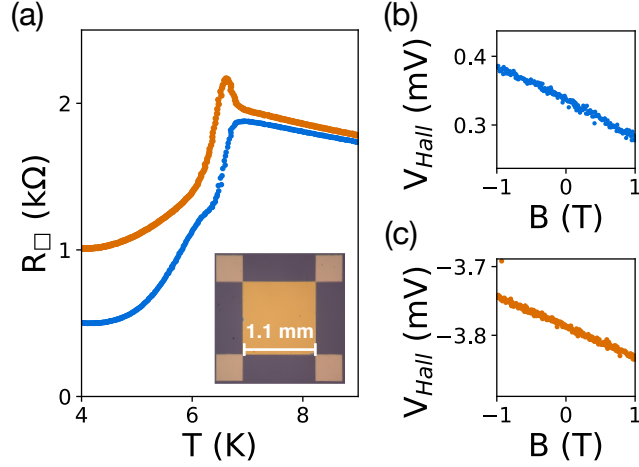


FIG. 5. a) Resistance per square (R_{\square}) vs. temperature (T) for the two devices on which Hall measurements were performed: device 1 (blue) and device 2 (orange). *Inset*: Optical image of a device lithographically identical to the ones on which the Hall measurements were performed. b)-c) Hall (transverse) voltage (V_{Hall}) vs. magnetic field (B) for device 1(2) at 8 K. A 10 μ A longitudinal current was sourced and a longitudinal voltage of 12.52(12.89) mV was measured at 0 T. The negative Hall slope shows that holes are the majority carrier. The carrier density of devices 1 and 2 were calculated to be (assuming the samples are uniform) 1.2×10^{14} and $1.4 \times 10^{14} \text{ cm}^{-2}$, respectively.

The lack of the expected symmetry of these Hall measurements about zero magnetic field could therefore suggest that the devices created in this material system are not uniform.

IV. DISCUSSION

A. Conductance changes due to external electric fields

The maximum change in resistance observed across the devices measured is less than 3% with gate-applied electric fields reaching 8 MV/cm. It is interesting to consider how much a 8 MV/cm electric field changes the hole carrier density in our devices, especially when compared to the hole carrier sheet density $h = 1.2 \times 10^{14} \text{ cm}^{-2}$ and $h = 1.4 \times 10^{14} \text{ cm}^{-2}$ measured by Hall measurements. If we assume a parallel capacitor model between the gate and channel in our devices, we calculate an expected change in hole carrier sheet density (δh) due to an external electric field (E) of $\delta h = \epsilon_r \epsilon_0 E / e$, where ϵ_0 is the permittivity in vacuum, $\epsilon_r = 3.9$ is the relative permittivity of SiO_2 and e is the electron charge. For an electric field of 8 MV/cm we get a change in hole carrier sheet

density $\delta h = 1.7 \times 10^{13} \text{ cm}^{-2}$ which is $\sim 13\%$ of the hole carrier sheet density measured by the Hall measurements.

We can also emphasize how small of a change 3% conductance change is by noting that a MOS-FET with a $d_{ox} = 30 \text{ nm}$ thick oxide and a $d_d = 1 \text{ nm}$ thick depletion layer has a sub-threshold slope of 62 mV/dec at 10 K (note that an idealized MOSFET would have $d_{ox} \ll d_d$ and the sub-threshold slope approaches 2 mV/dec at 10 K²⁶). A 62 mV change in top gate voltage of such a transistor would change the source drain resistance by an order of magnitude. If we assume we could change the conductance of our devices by 3% with an 8 MV/cm field, then to change the resistance of the Si:Ga devices reported here by an order of magnitude electric fields more than 100 times stronger than those we have already applied would be required. We note that the highest reported breakdown fields we could find for SiO₂ films is around 27 MV/cm²⁷, less than 4 times higher than the 8 MV/cm breakdown field measured here. Since strong external electric fields (of up to 8 MV/cm) are only able to change the conductivity of these samples by less than 3% and carrier density by $\sim 13\%$, this material system is not promising for voltage-gateable superconductivity.

B. Resistance variations below T_C and inhomogeneity

We note that the STEM images in figure 4(c) show that the devices reported here are inhomogeneous on the scale of tens of nm (the size of the gallium nano-precipitates). Substantial inhomogeneity is also observed on a macroscopic scale, as the resistance of nominally identical samples varies by many orders of magnitude below the superconducting transition. One possible explanation for this behavior is that the gallium nano-precipitates at the Si/SiO₂ interface are superconducting but that the conductance between these precipitates, or a precipitate network, varies. This could either be caused by varying doping levels of the material between the precipitates or by a variation in the density of the precipitates.

V. CONCLUSION

Motivated by the gateability of the proximity effect in III-V materials^{2,4,5}, II-VI materials⁶ and germanium^{7,22}, we sought to determine whether the well-established superconductivity in silicon doped with gallium^{15–21} is also gateable. With a goal of identifying a method for establishing

gateable superconductivity in gallium-doped silicon, we prepared and measured a series of samples with different annealing protocols and measured their conductivity. We saw less than a 3% change in device conductance when applying external electric fields, even when applying fields of up to 8 MV/cm.

In nominally identical devices measured at liquid helium temperatures (below the superconducting transition), we measured a variability of many orders of magnitude in the resistance. Such variation is even found in nominally identical devices located on the same die, indicating that this material system is inhomogeneous on a macroscopic scale.

We showed that the superconductivity is only present in the gallium rich layer at the Si/SiO₂ interface in these samples: Completely removing the gallium in this layer resulted in a resistance that continued to rise as the temperature was lowered below T_C .

The less than 3% change in device conductance when applying external electric fields and the many order-of-magnitude variation in device resistances at $T = 4.2$ K below the superconducting transition leads us to conclude that this material system is not a promising system for voltage-gateable superconductivity.

ACKNOWLEDGEMENTS

The authors acknowledge helpful discussions with J. C. McCallum, R. F. McDermott, D. E. Savage, Viktoriia Kornich, Mark Friesen, M. G. Vavilov and A. Levchenko. We acknowledge Song Jin for allowing us use of his PPMS. The data that support the findings of this study are available from the corresponding author upon reasonable request.

This work was supported in part by NSF EAGER under Grant No. DMR-1743986 and the Vannevar Bush Faculty Fellowship program sponsored by the Basic Research Office of the Assistant Secretary of Defense for Research and Engineering and funded by the Office of Naval Research through Grant No. N00014-15-1-0029, and by the Army Research Office (W911NF-17-1-0274). The views and conclusions contained in this document are those of the authors and should not be interpreted as representing the official policies, either expressed or implied, of the Army Research Office (ARO), or the U.S. Government. The U.S. Government is authorized to reproduce and distribute reprints for Government purposes notwithstanding any copyright notation herein. The authors gratefully acknowledge use of facilities and instrumentation at the UW-Madison Wisconsin Centers for Nanoscale Technology (wcnt.wisc.edu) partially supported by the NSF through

APPENDICES

Appendix A: Correlation between resistance at $T = 4.2$ K below T_C and I_C

Figures 6(a)-(c) show sourced current vs. measured voltage for 3 nominally identical devices annealed at 550°C for 30 s and measured in liquid helium (at 4.2 K), on a lin-lin plot and figures 6(d)-(f) show the same data, on a log-log plot. Each plot has the same range and dimensions. For each measurement the critical current, I_C , at which the voltage increase becomes superlinear with increased current, is marked. A black line, corresponding to a linear relationship of the voltage measured to the current for currents below half I_C , is also shown, and we call this slope the resistance at $T = 4.2$ K. For samples with a high resistance at $T = 4.2$ K the voltage change eventually becomes linear again. For devices with low resistance at $T = 4.2$ K this superlinear voltage change with current has not stopped within the measurement range of the experiment. Figure 6(g) shows the resistance at $T = 4.2$ K vs. I_C for 21 nominally identical devices. The resistance at $T = 4.2$ K of these devices varies by more than 5 orders of magnitude while the critical current varies by an order of magnitude, even though these devices are nominally identical, some even located on the same $5 \times 5 \text{ mm}^2$ die.

We will now argue why the current at which the voltage behaviour becomes superlinear with current can be called the critical current even though the resistance of the devices is not zero below this current value, by modeling our system as a network of superconductors and normal resistors. Let us limit our discussion to a simple network, an ensemble of superconductors and resistors connected in series. We denote the resistance of each normal resistor r_{nn} , the total normal resistance $R_{nn} = \sum r_{nn}$, the normal state resistance of each superconductor r_{sn} , and the total normal state resistance of the superconductors $R_{sn} = \sum r_{sn}$. If all the superconductors have the same critical current then we would expect the resistance of the network to change from R_{nn} to $R_{nn} + R_{sn}$ when the critical current is exceeded. However, the precipitates vary in size, so we expect their critical currents to also vary. Then instead of a sharp transition at a single current value from R_{nn} to $R_{nn} + R_{sn}$ we would expect the resistance to be R_{nn} below the lowest critical current and then start increasing as we go through the different critical current values of the precipitates, eventually reaching $R_{nn} + R_{sn}$ as we exceed the highest critical current value. According to this model, what we

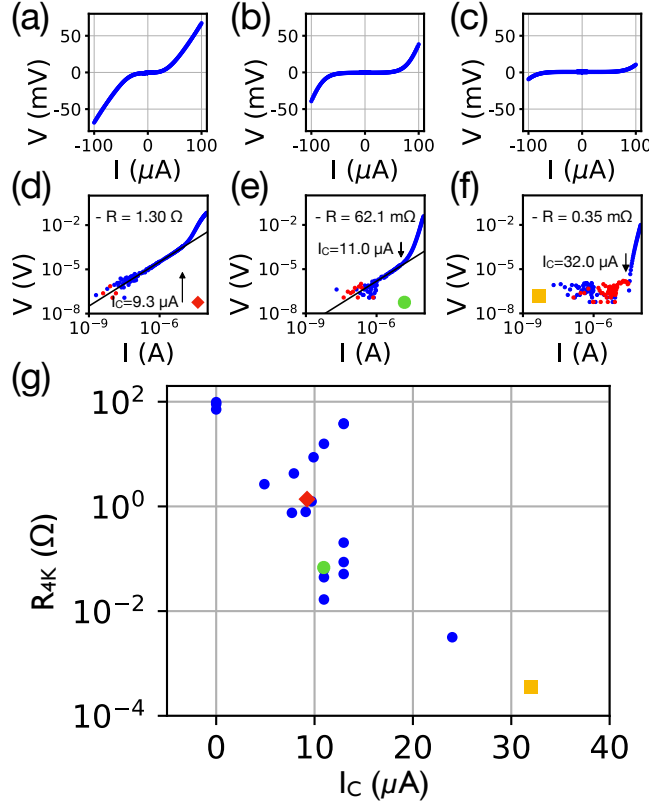


FIG. 6. Correlation between resistance at $T = 4.2$ K and critical current for the nominally identical devices, annealed at 550°C for 30 s, corresponding to figure 3 above. (a)-(c) Voltage vs. current measurements of 3 nominally identical devices. (d)-(f), Same data as in (a)-(c) plotted on a log-log scale. For each dataset the critical current, I_C , is marked. Values where a negative voltage, below the noise floor ($|V| < 1 \mu\text{V}$), was measured are colored red. The resistance, indicated by the solid black line, is determined as the coefficient of a linear form of the data below $I_C/2$. For (f) (the sample with the lowest resistance) the resistance is less than $R = V/I(I_C) = 0.35 \text{ m}\Omega$. (g) The resistance at $T = 4.2$ K vs. I_C , acquired by repeating the above procedure for 21 nominally identical devices. The results for (d), (e) & (f) are identified by a red diamond, a green circle and a yellow square respectively. The resistances of these nominally identical devices varies by more than 5 orders of magnitude, while the critical current varies by an order of magnitude. This variation is even shown in devices fabricated on the same die.

have called the critical current in figure 6 is the lowest critical current of superconducting gallium nano-precipitates in the network.

Appendix B: Final oxide thicknesses

As discussed in section II A all devices had nominally 30 nm of SiO₂ sputtered onto them before the Ga ion implantation and during the ion implantation a portion of this oxide is ablated. Furthermore, different amounts of additional gate oxide were added during subsequent processing for different devices. Determining the final oxide thickness is important in order to accurately determine the applied external electric field from the applied top gate voltage. For devices where the additional gate oxide was comparable to the initial 30 nm of SiO₂ sputtered prior to the Ga ion implantation, scanning transmission electron microscope (STEM) images were used to determine the final oxide thickness (the preparation and imaging of STEM samples is discussed section II B). From these STEM images we can determine that most of the sputtered oxide is ablated during the ion implantation (see figure 1(e)). For devices where the additional gate oxide was thicker (≥ 100 nm) than the initial 30 nm of SiO₂ sputtered oxide we use the result that most of the sputtered oxide is ablated during the ion implantation, and assume that the final oxide thickness can be approximated, within $\sim 10\%$, by the thickness of the additional oxide. Finally, we note that as we only observe negligible changes in device resistances with applied external electric fields, accurately determining the value of the external field is not critical to the results shown nor the conclusions drawn in this paper.

REFERENCES

- ¹Silvano De Franceschi, Leo Kouwenhoven, Christian Schönenberger, and Wolfgang Wernsdorfer. Hybrid superconductor–quantum dot devices. *Nature Nanotechnology*, 5(10):703–711, 2010.
- ²T. W. Larsen, K. D. Petersson, F Kuemmeth, T. S. Jespersen, P Krogstrup, J Nygård, and C. M. Marcus. Semiconductor-Nanowire-Based Superconducting Qubit. *Physical Review Letters*, 115(12):127001, 2015.
- ³Yun Pil Shim and Charles Tahan. Superconducting-semiconductor quantum devices: From qubits to particle detectors. *IEEE Journal of Selected Topics in Quantum Electronics*, 21(2):1–9, 2015.
- ⁴Yong-Joo Doh, Jorden A van Dam, Aarnoud L Roest, Erik P A M Bakkers, Leo P Kouwenhoven, and Silvano De Franceschi. Tunable Supercurrent Through Semiconductor Nanowires. *Science*, 309(5):272–275, 2005.

- ⁵Hao Zhang, Chun-Xiao Liu, Sasa Gazibegovic, Di Xu, John A Logan, Guanzhong Wang, Nick van Loo, Jouri D S Bommer, Michiel W A de Moor, Diana Car, Roy L M Op het Veld, Petrus J van Veldhoven, Sebastian Koelling, Marcel A Verheijen, Mihir Pendharkar, Daniel J Pennachio, Borzoyeh Shojaei, Joon Sue Lee, Chris J Palmstrøm, Erik P A M Bakkers, S Das Sarma, and Leo P Kouwenhoven. Quantized Majorana conductance. *Nature*, 556(7699):74–79, 2018.
- ⁶Sean Hart, Hechen Ren, Michael Kosowsky, Gilad Ben-Shach, Philipp Leubner, Christoph Brüne, Hartmut Buhmann, Laurens W. Molenkamp, Bertrand I. Halperin, and Amir Yacoby. Controlled finite momentum pairing and spatially varying order parameter in proximitized HgTe quantum wells. *Nature Physics*, 13(1):87–93, 2017.
- ⁷N. W. Hendrickx, D. P. Franke, A. Sammak, M. Kouwenhoven, D. Sabbagh, L. Yeoh, R. Li, M. L. V. Tagliaferri, M. Virgilio, G. Capellini, G. Scappucci, and M. Veldhorst. Gate-controlled quantum dots and superconductivity in planar germanium. *Nature Comm.*, 9(2835), 2018.
- ⁸Morten Kjaergaard, Konrad Wölms, and Karsten Flensberg. Majorana fermions in superconducting nanowires without spin-orbit coupling. *Physical Review B*, 85(2):20503–20504, 2012.
- ⁹L.N. Maurer, J.K. Gamble, L. Tracy, S. Eley, and T.M. Lu. Designing Nanomagnet Arrays for Topological Nanowires in Silicon. *Physical Review Applied*, 10(5):054071, 2018.
- ¹⁰Sara Turcotte, Samuel Boutin, Julien Camirand Lemyre, Ion Garate, and Michel Pioro-Ladrière. Optimized micromagnet geometries for Majorana zero modes in low g-factor materials. arXiv:1904.06275.
- ¹¹G. W. Gobeli and F. G. Allen. Photoelectric Properties of Cleaved GaAs, GaSb, InAs, and InSb Surfaces; Comparison with Si and Ge. *Physical Review*, 137(1A):A245–A254, 1965.
- ¹²W. M. Van Hufelen, T. M. Klapwijk, and L. De Lange. Nonequilibrium carrier transport in superconducting niobium-silicon heterostructures. *Physical Review B*, 45(1):535–538, 1992.
- ¹³W. M. Van Hufelen, T. M. Klapwijk, D. R. Heslinga, M. J. De Boer, and N. Van Der Post. Carrier transport in mesoscopic silicon-coupled superconducting junctions. *Physical Review B*, 47(9):5170–5189, 1993.
- ¹⁴E Bustarret, C Marcenat, P Achatz, J Kačmarčík, F Lévy, A Huxley, L Ortéga, E Bourgeois, X Blase, D Débarre, and J Boulmer. Superconductivity in doped cubic silicon. *Nature*, 444(7118):465–468, 2006.
- ¹⁵R Skrotzki, J Fiedler, T Herrmannsdörfer, V Heera, M Voelskow, A Mücklich, B Schmidt, W Skorupa, G Gobsch, M Helm, and J Wosnitza. On-chip superconductivity via gallium overdoping of silicon. *Applied Physics Letters*, 97(19):192503–192505, 2010.

- ¹⁶J Fiedler, V Heera, R Skrotzki, T Herrmannsdörfer, M Voelskow, A Mücklich, S Oswald, B Schmidt, W Skorupa, G Gobsch, J Wosnitza, and M Helm. Superconducting films fabricated by high-fluence Ga implantation in Si. *Physical Review B*, 83(21):205–210, 2011.
- ¹⁷V Heera, J Fiedler, M Voelskow, A Mücklich, R Skrotzki, T Herrmannsdörfer, and W Skorupa. Superconductor-insulator transition controlled by annealing in Ga implanted Si. *Applied Physics Letters*, 100(26):262602–262604, 2012.
- ¹⁸T Fischer, A V Pronin, R Skrotzki, T Herrmannsdörfer, J Wosnitza, J Fiedler, V Heera, M Helm, and E Schachinger. Optical study of superconducting Ga-rich layers in silicon. *Physical Review B*, 87(1):14502–14505, 2013.
- ¹⁹V Heera, J Fiedler, R Hübner, B Schmidt, M Voelskow, W Skorupa, R Skrotzki, T Herrmannsdörfer, J Wosnitza, and M Helm. Silicon films with gallium-rich nanoinclusions: from superconductor to insulator. *New Journal of Physics*, 15(8):83015–83022, 2013.
- ²⁰V Heera, J Fiedler, B Schmidt, R Hübner, M Voelskow, R Skrotzki, and W Skorupa. Negative Magneto and Electroresistance of Silicon Films with Superconducting Nanoprecipitates: The Role of Inelastic Cotunneling. *Journal of Low Temperature Physics*, 180(5):342–355, 2015.
- ²¹V Heera, J Fiedler, and W Skorupa. Resistance fluctuations in insulating silicon films with superconducting nanoprecipitates – superconductor-to-metal or vortex matter phase transition? *AIP Advances*, 5(11):117217–117219, 2015.
- ²²J Xiang, A Vidan, M Tinkham, R M Westervelt and Charles M Lieber. Ge/Si nanowire mesoscopic josephson junctions *Nature Nanotechnology*, 1(3):208–213, 2006.
- ²³*Low Level Measurement Handbook*. Keithley Instruments, Cleaveland, 7 edition, 2013.
- ²⁴V Heera, J Fiedler, and W Skorupa. Large magnetoresistance of insulating silicon films with superconducting nanoprecipitates *AIP Advances*, 6(10):105203-105209, 2016.
- ²⁵E Nygren, J C McCallum, R Thornton, J S Williams, and G L Olson. Amorphous to Polycrystalline Transformation in High Dose Ion Implanted Silicon. *MRS Proceedings*, 100:405–409, 1988.
- ²⁶Arnout Beckers, Farzan Jazaeri, and Christian Enz. Cryogenic MOS Transistor Model. *IEEE Transactions on Electron Devices*, 65(9):3617–3625, 2018.
- ²⁷Takane Usui, Christine A. Donnelly, Manca Logar, Robert Sinclair, Joop Schoonman, and Fritz B. Prinz. Approaching the limits of dielectric breakdown for SiO₂ films deposited by plasma-enhanced atomic layer deposition. *Acta Materialia*, 61(20):7660–7670, 2013.